Research Square

Preprints are preliminary reports that have not undergone peer review.
They should not be considered conclusive, used to inform clinical practice,
or referenced by the media as validated information.

Phenome-wide associations of CT-derived adipose area and density in 22,710 patients: uncovering unexpected disease connections

Ates Fettahoglu

atesfet@stanford.edu

Stanford University https://orcid.org/0000-0003-1652-4469

Juan Zambrano Chaves

Microsoft Research

Andrea Fisher

Stanford University

Ivan Lopez

Stanford University https://orcid.org/0000-0003-0246-2180

Tie Liang

Stanford University

Robert Holland

Stanford University

Saaket Agrawal

Stanford University

George Nageeb

Stanford University

Ashwin Kumar

Stanford University

Curtis Langlotz

Stanford University https://orcid.org/0000-0002-8972-8051

Alexander Sandhu

Stanford Medicine

David Maron

Stanford University https://orcid.org/0000-0002-4867-8588

Fatima Rodriguez

Stanford University https://orcid.org/0000-0002-5226-0723

Leon Lenchik

Stanford University

Akshay Chaudhari

Stanford University

Robert Boutin

Stanford University https://orcid.org/0000-0001-7887-9658

Article

Keywords: Adipose tissue, Biomarker discovery, Cardiovascular-kidney-metabolic syndrome, Computed tomography, Electronic health records, Phenome-wide association study, Deep learning, Opportunistic screening

Posted Date: November 20th, 2026

DOI: https://doi.org/10.21203/rs.3.rs-11406927/v1

License: This work is licensed under a Creative Commons Attribution 4.0 International License. Read Full License

Additional Declarations: There is **NO** Competing Interest.

Phenome-wide associations of CT-derived adipose area and density in 22,710 patients: uncovering unexpected disease connections

Ates Fettahoglu[1,2], Juan M. Zambrano Chaves[3], Andrea Fisher[1,2,4], Ivan Lopez[5,6], Tie Liang[2], Robbie Holland[1,2], Saaket Agrawal[6,7,8], George Nageeb[6,9], Ashwin Kumar[1,2], Curtis P. Langlotz[1,2], Alexander T Sandhu[10,11], David J. Maron[12], Fatima Rodriguez[13], Leon Lenchik[2], Akshay S. Chaudhari[2,5]§, Robert D. Boutin[2]§

§ASC and RDB are co-senior authors

[1]Stanford Center for Artificial Intelligence in Medicine and Imaging, Stanford, CA, USA

[2]Department of Radiology, Stanford University, Stanford, CA, USA

[3]Microsoft Research, Redmond, WA, USA

[4]Stanford Division of Vascular Surgery, Department of Surgery, Stanford, CA, USA

[5]Department of Biomedical Data Science, Stanford University, Stanford, CA, USA

[6]Department of Medicine, Stanford University School of Medicine, Stanford, CA, USA

[7]Division of Cardiovascular Medicine, Stanford University, Stanford, CA, USA

[8]Cardiovascular Institute and Center for Inherited Cardiovascular Disease, Stanford, CA, USA

[9]Department of Neurosurgery, Stanford University, Stanford, CA, USA

[10]Division of Cardiology, Department of Medicine, University of California Los Angeles, Los Angeles, CA, USA

[11]Greater Los Angeles Veterans Affairs Healthcare System, Los Angeles, CA, USA

[12]Stanford Prevention Research Center and Division of Cardiovascular Medicine, Stanford, CA, USA

[13]Division of Cardiovascular Medicine, the Cardiovascular Institute, and the Center for Digital Health, Stanford University School of Medicine, Stanford, CA, USA

Abstract

Adipose tissue plays a central role in metabolic and inflammatory homeostasis, yet its quantity and composition are rarely characterized together in routine care. We performed a phenome-wide association study linking abdominal CT scans from 22,710 patients at two tertiary care centers to electronic health record phenotypes. Subcutaneous and visceral fat area indices (SFI, VFI) and densities (SFD, VFD) were derived with a validated deep learning pipeline and tested against 624 phenotypes (2,496 tests). We identified 922 Bonferroni-significant associations across 60% (373/624) of phenotypes, recapitulating established relationships with morbid obesity (SFI odds ratio [OR] = 1.60), type 2 diabetes (VFI OR = 1.57), cirrhosis (VFD OR = 3.56) and pancreatic cancer (SFI OR = 0.56). Across the phenome, area and density odds ratios were inversely correlated (r = −0.80), as expected for markers inversely correlated within each depot. When modelled jointly, density remained associated with disease independently of area for 90% (351/392) of phenotypes with a joint adipose association, whereas area was informative beyond density for 35% (136/392) and without density for 2% (6/392). These findings provide a hypothesis-generating atlas in which adipose density emerges as a candidate biomarker of systemic physiology. All analysis code and results are openly available (https://atesfet.github.io/fatwas.io).

Abbreviations: Body Mass Index (BMI); Cardiovascular-Kidney-Metabolic (CKM); Confidence Interval (CI); Computed Tomography (CT); Electronic Health Records (EHR); Glucagon-Like Peptide-1 Receptor Agonists (GLP-1RAs); Hounsfield Units (HU); International Classification of Diseases (ICD); Lumbar Vertebra 3 (L3); Odds Ratio (OR); Phenome-Wide Association Study (PheWAS); Picture Archiving and Communications System (PACS); Subcutaneous Fat Density (SFD); Subcutaneous Fat Index (SFI); Visceral Fat Density (VFD); Visceral Fat Index (VFI)

Keywords: Adipose tissue, Biomarker discovery, Cardiovascular-kidney-metabolic syndrome, Computed tomography, Electronic health records, Phenome-wide association study, Deep learning, Opportunistic screening.

Introduction

Recent work has emphasized adipose tissue as a central component of organismal aging[1] and dysfunctional adiposity driving cardiovascular-kidney-metabolic syndrome (CKM)[2]. The opportunity to directly target obesity with glucagon-like peptide-1 receptor agonists (GLP-1RAs) further emphasizes the importance of better understanding adipose tissue[3]. Beyond promoting weight loss, GLP-1RAs and dual incretin agonists have been reported to improve hepatic steatosis and liver inflammation in clinical and preclinical studies[4–6]. The systemic effects of adipose tissue reduction suggest that the extent and composition of the adipose tissue may carry important metabolic and systemic implications beyond total fat mass[6–8]. These developments highlight the growing need to characterize not only the amount of fat, but also its biological properties and systemic correlates.

Advances in automated CT image analysis have enabled large-scale, quantitative phenotyping of diseases from routine clinical imaging. Abdominal CT provides high-resolution assessment of body composition. CT-derived adipose area and density are widely used as imaging biomarkers across diverse disease domains[9–17]. Prior CT studies primarily assess adipose tissue morphology using area or volume[18–20], consistently showing that excess visceral adiposity is associated with adverse cardiometabolic outcomes[21–23]. More recently, the CKM syndrome framework has emphasized dysfunctional adiposity as an early pathophysiological driver linking obesity with cardiovascular disease, chronic kidney disease, and metabolic risk factors[2]. Emerging evidence suggests that CT-derived adipose density may reflect differences in lipid content, inflammation, and fibrosis[9,24–26], but these relationships have largely been examined one disease or cohort at a time, and how density

relates to disease across the broader clinical phenome remains unexplored. Lower adipose density (lower Hounsfield units [HU]) has been linked to larger adipocytes with higher lipid content, whereas higher adipose density has been linked to increased water content, inflammatory cell infiltration, or fibrosis[26,27], which may indicate a shift from energy storage to a pro-inflammatory and metabolically stressed phenotype[28,29]. Furthermore, independent of adipose area, adipose density may reflect systemic metabolic changes that have been associated with hepatic steatosis, CKM syndrome, and mortality.[10,11,15,25,30]

Phenome-wide association studies (PheWAS) offer a scalable strategy to link biomarkers with a wide array of medical conditions derived from electronic health records (EHR). PheWAS can systematically test associations between a single primary variable of interest, such as an imaging biomarker, and a broad spectrum of clinical phenotypes to identify both known and not previously described disease relationships. Originally applied to genetic variants,[31] PheWAS methodology has since been adapted to clinically defined disease subgroups[32,33] and, more recently, to imaging-derived muscle metrics for investigating myopenia and myosteatosis, and to brown adipose tissue detected on routine clinical imaging, linking its presence to a lower prevalence of cardiovascular and psychiatric diseases.[34,35] Applying such approaches to adipose tissue could enable simultaneous validation of known associations and discovery of previously unrecognized systemic relationships, generating mechanistic hypotheses and informing downstream study design[34].

In this work, we apply imaging–PheWAS methodology to adipose tissue by analyzing 22,710 clinical abdominal CT scans linked to phenotypes available in the EHR. Specifically,

we derive four fat measures using a validated deep learning pipeline: two morphological metrics, subcutaneous fat index (SFI) [cm2/m] and visceral fat index (VFI) [cm2/m], and two compositional metrics, subcutaneous fat density (SFD) [HU] and visceral fat density (VFD) [HU]. We then test their associations with 624 medical phenotypes derived from 11,742 unique ICD codes, as well as all-cause mortality. We hypothesized that such large-scale phenome-wide analysis of the morphological and compositional characteristics of subcutaneous and visceral adiposity can reveal new insights across diverse disease domains. Our study provides a comprehensive resource for understanding the multisystem relevance of adipose tissue characteristics, with results that can inform and guide future mechanistic and prospective clinical research. An interactive version of these results is available on a website (https://atesfet.github.io/fatwas.io/), where all phenome-wide associations can be explored in detail.

Results

CT-derived adipose metrics reveal sex- and age-dependent variation in adipose area and density

To characterize the distribution of CT-derived adipose biomarkers across our study population, we quantified SFI, VFI, SFD, and VFD from contrast-enhanced abdominal CT scans in 22,710 adults at two tertiary care academic medical centers. The mean age was 56.3 ± 18.3 years, and 57.8% were female (Table 1). Men exhibited substantially higher VFI values (101.2 ± 67.7 cm^2/m vs. 67.0 ± 51.8 cm^2/m, p<0.0001), whereas SFI was greater in women (146.9 ± 91.4 cm^2/m vs. 99.8 ± 64.4 cm^2/m, p<0.0001). SFD was lower in women (−96.3 ± 13.4 HU vs. −92.8 ± 14.9 HU, $p < 0.0001$), while VFD was higher (−81.5 ± 12.3 HU vs.

−83.5 ± 13.0 HU, $p < 0.0001$) (Table 1). Across age strata, SFI peaked in early adulthood and declined thereafter (women, 165.0 cm^2/m at 30–39 years; men, 110.7 cm^2/m at 40–49 years), whereas VFI rose progressively across the lifespan to a late peak in the eighth decade (women, 79.6 cm^2/m; men, 119.9 cm^2/m) before declining. Adipose density was highest at the extremes of age, with a nadir in midlife. Subcutaneous density peaked in the oldest stratum and visceral density in the youngest, although subcutaneous density in young women was not elevated (Table 2).

Phenome-wide analysis identifies 922 associations across 373 phenotypes spanning 14 disease groups

To systematically map the disease associations of adipose area index and density metrics across the clinical phenome, we performed a phenome-wide association study of 624 phecode-defined phenotypes derived from the EHR (2,496 marker–phenotype tests in total), adjusting for age, sex, BMI, and CT scanner parameters of tube current, tube voltage, and slice thickness. The study design is given in Figure 1. Among the 624 phenotypes tested, the categories with the highest mean phenotype prevalence were symptoms (9.6% [95% CI: 2.5-16.7]), digestive disorders (6.4% [95% CI: 5.1-7.7]), mental disorders (5.9% [95% CI: 4.0-7.8]), and endocrine/metabolic disorders (5.7% [95% CI: 4.1-7.3]) (Table 3). Using a conservative Bonferroni-corrected threshold ($p < 0.05/2{,}496 = 2.0 \times 10^{-5}$), 922 phenotype associations were identified across 373 phenotypes in 14 of the 16 tested disease groups. 81 phenotypes were associated with all four adipose metrics, while 82, 142, and 68 phenotypes were associated with three, two, and one metric, respectively. Volcano plots of odds ratios (OR) versus significance for all respective metrics are given in Figure 2.

CT-derived adipose metrics recapitulate established metabolic disease associations

To establish construct validity of our imaging-PheWAS framework, we assessed whether CT-derived adipose metrics reproduced known associations with metabolic conditions for which adiposity relationships are firmly established. Odds ratios are expressed per one sex-specific standard-deviation increase in each metric.

As expected, morbid obesity was significantly associated with all four adipose metrics (SFI OR = 1.60 [95% CI 1.47–1.75], $p < 0.0001$; VFI OR = 1.29 [95% CI 1.19–1.40], $p < 0.0001$; SFD OR = 1.91 [95% CI 1.74–2.08], $p < 0.0001$; VFD OR = 1.51 [95% CI 1.38–1.65], $p < 0.0001$) (Table 4). Type 2 diabetes was significantly associated with VFI (OR = 1.57 [95% CI 1.50–1.66], $p < 0.0001$) and SFD (OR = 1.32 [95% CI 1.26–1.38], $p < 0.0001$), whereas SFI and VFD did not reach Bonferroni significance.

Liver, oncologic, catabolic and decompensated states show lower adipose area with higher adipose density

Cirrhosis was associated with all four adipose metrics, with inverse area associations and positive density associations (SFI OR = 0.46 [95% CI 0.40–0.53]; VFI OR = 0.70 [95% CI 0.63–0.78]; SFD OR = 2.90 [95% CI 2.68–3.14]; VFD OR = 3.56 [95% CI 3.26–3.90]; all $p < 0.0001$). Other hepatic phenotypes, portal hypertension and the composite phecode "liver abscess and sequelae of chronic liver disease," showed the same pattern of lower adipose area and higher adipose density, as did end-stage kidney disease, pancreatic cancer, and protein-calorie malnutrition. For end-stage kidney disease and pancreatic cancer, VFI did not reach Bonferroni significance. The largest effects among these phenotypes were the positive association of portal hypertension with VFD (OR = 5.28) and

the inverse association of protein-calorie malnutrition with SFI (OR = 0.29). Odds ratios and 95% CIs for these phenotypes are in Table 4; all associations are available online. In these severe hepatic, renal, oncologic, and catabolic conditions, higher adipose density occurred together with lower adipose area.

By making these findings openly accessible, we aim to facilitate hypothesis generation, independent validation, and downstream mechanistic investigations by the broader research community.

Directional discordance between area and density

Area- and density-based adipose biomarkers demonstrated markedly different phenome-wide association profiles (summarized in Figure 3). Of the 922 Bonferroni-significant marker–phenotype associations, 655 (71.0%) involved density markers, compared with 267 (29.0%) involving area markers. Similarly, density was associated with 365 phenotypes, whereas area was associated with 186. Among the 373 phenotypes with at least one significant association, 187 (50.1%) were density-only, 8 (2.1%) were area-only, and 178 (47.7%) were associated with both biomarker classes. Density therefore accounted for 2.5-fold more significant associations than area, and few phenotypes were identified by area alone: only 8 phenotypes were area-exclusive, against 187 that were density-exclusive. Density-only associations occurred in all 14 disease groups with a significant association (of 16 tested), whereas area-only associations occurred in only four. The density-only signal was particularly prominent in circulatory disease (45 phenotypes), digestive disease (26), neoplasms (19), and endocrine/metabolic disease and injuries and poisonings (12 each),

demonstrating that the greater yield of density associations was not restricted to a single organ system.

The 178 phenotypes associated with both area and density were classified as directionally concordant when the strongest area and density associations were on the same side of the null and as directionally discordant when they were on opposite sides with respect to their odds ratio. Only 14 of 178 overlapping phenotypes (7.9%) were concordant, whereas 164 (92.1%) were directionally discordant. For most of these phenotypes, the disease was associated with less adipose tissue of higher density, and the conventional pattern of more adipose tissue accompanying more disease was largely confined to the small cardiometabolic subset described below. Because area and density are inversely correlated within each depot (SFI–SFD $r = -0.40$, $p < 0.0001$; VFI–VFD $r = -0.65$, $p < 0.0001$), opposite-signed associations are expected whenever a disease tracks a single adiposity axis, so directional discordance alone does not show that the two classes carry separate information; we address this with joint models below. The discordant pattern was strongly asymmetric: 156 of 164 phenotypes combined a lower area-associated odds ratio with a higher density-associated odds ratio, whereas only 8 exhibited the reverse pattern (higher area-associated and lower density-associated odds ratio). The inversion was not confined to the phenotypes that reached significance for both classes: across all 624 tested phenotypes the representative area and density log odds ratios were strongly inversely correlated (Pearson $r = -0.80$, reported descriptively because phenotypes are nested and share patients), consistent with the inverse correlation of the markers themselves (Figure 3a). Portal hypertension exemplified this predominant discordance, with subcutaneous fat

index associated with reduced odds and visceral fat density associated with markedly increased odds (SFI OR = 0.38 versus VFD OR = 5.28; Table 4).

The much smaller concordant subset comprised nested phecodes for diabetes (6), obesity (3) and hypertension (3), together with coronary atherosclerosis and disorders involving the immune mechanism. All 14 concordant phenotypes had area and density odds ratios greater than 1, and none had both below 1. They were concentrated in endocrine/metabolic (10 phenotypes) and circulatory (4) disease groups (Figure 3a, upper-right quadrant). Manhattan plots of all phenome-wide associations with respect to each marker are shown in Figure 4.

Joint modelling separates adipose composition from adipose quantity

Because adipose area and density were correlated within each depot, single-marker models could not completely separate an association with adipose composition from one with adipose quantity. We therefore modelled all four markers jointly for each of the 624 phenotypes (Figure 5). The four markers were jointly associated with 392 phenotypes. These overlap with, but are not identical to, the 373 phenotypes identified in the single-marker analysis (371 in common), because the joint analysis tests all four markers together in one test per phenotype: 21 phenotypes reached significance only jointly, and 2 single-marker associations were not significant in the joint test. Density remained associated after adjustment for both area markers in 351 of these (89.5%), whereas area remained associated after adjustment for both density markers in 136 (34.7%); only 6 phenotypes had an area association without a density association, and for 35 the joint signal could not be attributed to either class (Figure 5c). Joint modelling changed the area associations most

(Figure 5a). Of the 137 phenotypes with a significant marginal SFI association, only 7 remained significant after adjustment for SFD. In contrast, all 160 phenotypes with a significant VFI association conditional on VFD had an odds ratio above 1. These included 108 whose marginal VFI odds ratio had been below 1 (56 of them significantly; for example, portal hypertension: VFI OR = 0.55 marginally and 2.88 [95% CI 2.45–3.38] conditional on VFD; Figure 5b). The density associations were largely unchanged (330 of 351 SFD and 282 of 304 VFD associations remained significant), and among the 359 phenotypes with a significant density marker conditional on its depot's area marker (depot-specific models), higher density was associated with higher odds for 336 and with lower odds for 23.

Higher adipose density and lower adipose area were associated with all-cause mortality

Among 22,710 participants, 2,692 deaths occurred over a median observed follow-up of 7.1 years (8.1 years at the first site and 1.9 years at the second). In models adjusted for age, sex, BMI, and CT acquisition parameters, each sex-specific standard-deviation increase in SFD was associated with higher odds of mortality at 1 year (OR = 2.05, 95% CI: 1.95–2.16, $p < 0.0001$) and 5 years (OR = 1.67, 95% CI: 1.59–1.75, $p < 0.0001$). Corresponding estimates for VFD were OR = 2.28 (95% CI: 2.14–2.43, $p < 0.0001$) and OR = 1.69 (95% CI: 1.60–1.78, $p < 0.0001$), respectively. Conversely, higher SFI was associated with lower mortality odds, and this inverse association attenuated markedly between the 1- and 5-year horizons: 1 year (OR = 0.47, 95% CI: 0.42–0.52, $p < 0.0001$) and 5 years (OR = 0.80, 95% CI: 0.73–0.87, $p < 0.0001$). VFI followed the same time course (1 year: OR = 0.62, 95% CI: 0.57–0.68, $p < 0.0001$; 5 years: OR = 0.89, 95% CI: 0.82–0.95, $p = 0.0009$). The density associations

also attenuated, but less than the area associations. Between the 1- and 5-year horizons the log odds ratio decreased by 29% for SFD and 37% for VFD, compared with 70% for SFI and 74% for VFI. Therefore, whereas the inverse area association with all-cause mortality was concentrated in the period immediately after imaging, the density association persisted, at reduced magnitude, through 5 years.

Discussion

We conducted a large-scale, retrospective phenome-wide association analysis linking CT-derived adipose tissue metrics with medical phenotypes derived from the EHR. Using 22,710 contrast-enhanced abdominal CT scans from adult patients at two distinct tertiary care hospitals, we quantified adipose area (SFI and VFI) and density (SFD and VFD) metrics using a validated deep learning pipeline. Associations were systematically tested across 624 distinct clinical phenotypes (2,496 marker–phenotype tests), adjusting for age, sex, BMI, tube current, tube voltage and slice thickness. Our phenome-wide analysis demonstrated that CT-derived adipose metrics capture a broad range of disease associations, characterizing cross-system relationships at scale. We reproduced expected associations (higher adipose area with obesity and type 2 diabetes; higher adipose density with cirrhosis, protein-calorie malnutrition, end-stage kidney disease and all-cause mortality), supporting the construct validity of both area and density metrics[13,34,36–43]. Although area metrics (SFI and VFI) identified phenotypes classically linked to excess adiposity, such as morbid obesity and type 2 diabetes, many of the strongest signals were observed for adipose density metrics (SFD and VFD): 79 of the 100 largest significant associations by absolute log odds ratio involved density.

For morbid obesity, higher values of all four markers were associated with higher odds of the diagnosis, and for type 2 diabetes higher VFI and SFD were (SFI and VFD were not significant). In contrast, for cirrhosis, portal hypertension, and end-stage kidney disease, lower fat area and higher fat density were associated with increased risk. This marginal discordance argues against interpreting these phenotypes simply as downstream "comorbidities" of obesity. In marginal models, obesity and type 2 diabetes were associated with higher adipose area and, at a given BMI, higher density, whereas advanced hepatic, kidney, infectious and gastrointestinal or metastatic malignant conditions were associated with lower adipose area and higher density, a pattern that could reflect catabolic, inflamed or edematous fat. This pattern is consistent with adipose density reflecting aspects of adipose tissue that differ from total fat burden. The two arms are not symmetric in strength: the inverse area associations of the catabolic phenotypes (for example SFI OR = 0.29 for protein-calorie malnutrition and 0.38 for portal hypertension) are considerably larger in magnitude than the positive area associations of the metabolic phenotypes (SFI OR = 1.60 for morbid obesity), although, because these models are adjusted for BMI, the positive area associations of the metabolic phenotypes are likely attenuated. Joint models refine this picture; the inverse area associations of the catabolic phenotypes were largely explained by density, and at a given visceral density a larger visceral area was associated with higher odds of these conditions. Among the density-associated phenotypes, the strongest associations included portal hypertension, cirrhosis, fluid overload, ascites, protein-calorie malnutrition and end-stage kidney disease (Table 4), alongside abdominal cancers, septic shock and respiratory failure. Higher adipose density has been linked to smaller adipocyte size in

309 catabolic states, including cachexia and pathologic weight loss, where reduced lipid
310 content increases CT attenuation[44]. Additionally, increased adipose tissue edema may
311 contribute to elevated attenuation in conditions such as decompensated cirrhosis, kidney
312 failure, or severe systemic illness[39,45]. The strong relationship between fat density and
313 malnutrition (a condition present in 45% of critically ill adults)[46] may reflect reduced oncotic
314 pressure from hypoalbuminemia, which promotes fluid extravasation into adipose and
315 other soft tissues.

316 The most prominent phenome-wide finding was that adipose density remained
317 associated with disease after adjustment for adipose area in 351 of the 392 phenotypes with
318 a joint adipose association (Figure 5c), whereas area was informative beyond density in 136
319 and, without density, in only 6; density also had the greater marginal association yield (655
320 versus 267 significant associations, and 187 versus 8 phenotypes identified exclusively by
321 one class). The few phenotypes for which area alone was informative were largely
322 metabolic, whereas density was associated with a broad range of conditions and most
323 strongly with acute, inflammatory and catabolic illness. Oncologic, hepatologic and critical-
324 care settings are therefore candidate settings in which to evaluate whether opportunistic
325 density assessment adds prognostic information beyond adipose quantity. Although the
326 biological mechanisms underlying these relationships remain uncertain, these findings
327 generate hypotheses for future mechanistic and longitudinal investigations examining the
328 systemic consequences of altered adiposity. This composition-based signal might also
329 contribute to the ability of deep learning models, including vision–language foundation
330 models, to forecast future cardiometabolic disease directly from abdominal CT. Models

trained to predict the multi-year incidence of conditions such as chronic kidney disease, diabetes, hypertension, and ischemic heart disease from routine scans[47,48] operate on the same images in which adipose composition is encoded, and the tissue-state information reflected in adipose density, rather than fat quantity alone, may be among the features such models implicitly leverage.

In our cohort, higher visceral and subcutaneous adipose density was strongly associated with greater mortality, whereas higher visceral and subcutaneous fat indices were associated with lower mortality. The inverse SFI association is consistent with evidence that subcutaneous adipose tissue can represent nutritional and metabolic reserve in older or medically complex populations. A dose–response meta-analysis of prospective cohorts in the general population found lower all-cause mortality per standard-deviation increase in subcutaneous adipose tissue, despite an adverse association for visceral adipose tissue[49]. Evidence regarding visceral adiposity is more conflicting. In a health-check cohort of 32,593 adults, greater subcutaneous fat area was associated with lower mortality, whereas greater visceral fat area and a higher visceral-to-subcutaneous ratio were associated with higher mortality, although only the ratio remained independently associated after multivariable adjustment[50]. A systematic review similarly found that greater visceral adipose area was generally associated with higher mortality in younger cohorts, although associations often attenuated after adjustment for variables such as BMI, other fat compartments, and glycaemic indices[51]. Visceral adiposity may therefore capture long-term risk in healthier populations, while low visceral area in clinically selected populations may also identify advanced illness, frailty, or catabolic tissue loss. Illness-related wasting

provides a plausible explanation for the early inverse area associations. Cachexia and chronic-disease wasting involve reduced intake, systemic inflammation, abnormal metabolism, increased lipolysis, and progressive depletion of muscle and adipose stores.[52–54] The early inverse associations of VFI and SFI may consequently reflect preserved energy reserve or less advanced catabolic illness rather than a direct benefit of greater adiposity. The time course of our estimates is compatible with this interpretation: the inverse association was strongest within the first year (SFI OR = 0.47) and attenuated toward the null by five years (OR = 0.80), as would be expected if prevalent wasting contributed to the early association, although this pattern does not by itself establish reverse causation.

Taken together, our findings position adipose density as a potentially informative biomarker of systemic physiology. At a population scale, modelling fat area and density across the phenome suggests different adipose signatures for metabolic disease and multisystem decompensation. CT scans obtained as part of routine medical care could, if validated, be used to complement existing approaches to evaluating fluid status, metabolic stress, or catabolic burden, especially in hospitalized or critically ill populations. In contrast to prior studies, our imaging pipeline spans a clinical population with a considerably broader array of diseases. This complements recent phenome-wide work on brown adipose tissue, in which the presence and activity of thermogenic fat were associated with a lower prevalence of cardiometabolic and psychiatric diseases and a healthier white fat distribution[35]. Brown adipose tissue, however, is assessed by its metabolic activity on ^{18}F-FDG PET/CT, an examination performed predominantly for oncologic indications, in which detection of active brown fat also depends on factors such as ambient temperature[55,56].

White adipose tissue area and density, in contrast, can be measured on routine CT acquired for a much wider range of clinical indications, allowing adipose phenotypes to be studied in a broader clinical population, albeit one still selected by the indication for imaging. Moreover, our imaging protocol offered substantially higher spatial resolution, allowing depiction of more subtle findings without confounders such as partial-volume effects (UK Biobank MRI protocol had voxel resolution of 17 mm^3 compared with our ~40x higher resolution of ~0.4 mm^3)[57]. Our segmentation model and analysis pipeline are open source (Comp2Comp; https://github.com/stanfordmimi/comp2comp), enabling other groups to replicate these analyses in their own cohorts.

Several limitations merit consideration. PheWAS methodology identifies associations rather than causal relationships, and some statistically significant findings may reflect heterogeneity in diagnosis, healthcare utilization, or coding practices. Further, we used a conservative Bonferroni correction for multiple comparisons which may obscure true associations with smaller effect sizes. Phenotypes with limited clinical specificity yield less interpretable associations. The BMI used for adjustment was the most recent value recorded in the EHR rather than a measurement at the time of imaging, obtained a median of 4.0 and 0.9 years after the CT at the two sites, and at one site the diagnosis window was offset by a median of about two weeks because of date shifting in the de-identified records. Diagnoses were mapped with Phecode Map v1.2, which predates several later ICD-10-CM revisions, so codes absent from the map were assigned to their nearest mapped parent code. Conditional estimates from joint models separate correlated exposures statistically rather than biologically, and the cross-sectional diagnosis window allows reverse

causation; the associations reported here are therefore hypothesis-generating and require external replication. Nevertheless, the consistency of validated associations, the systematic emergence of biologically plausible density-related findings, and the robustness of the imaging pipeline reinforce the credibility of the observed patterns.

In summary, this study extends PheWAS methodology to adipose tissue and reveals that adipose density, in tandem with area metrics, captures a multidimensional signature of systemic disease. The persistence of density associations after adjustment for adipose area, in 351 of the 392 phenotypes with a joint adipose association, indicates that adipose density captures information complementary to area. The adipose density associations identified in this study, including those involving hepatic decompensation, kidney dysfunction, and severe infection, highlight the potential of adipose density as an opportunistic marker of multisystem physiologic stress. Future longitudinal and mechanistic studies will be essential to define causal pathways underlying these relationships and to explore opportunities for clinical intervention. Together, these results constitute a hypothesis-generating atlas of adipose–disease associations to guide replication and mechanistic study.

Methods

Study design

We conducted an institutional review board (IRB)-approved retrospective cohort study using a PheWAS framework to identify associations between abdominal CT–derived fat metrics (SFI, VFI, SFD, VFD) and medical phenotypes. Automated segmentation and quantitative imaging biomarkers were derived from contrast-enhanced abdominal CT

scans, and diagnostic codes from the EHR were mapped to standardized phenotypes (phecodes) for association analysis.

Data sources and study population

This study used imaging and clinical data from two separate tertiary care hospitals obtained under IRB approval with a waiver of patient consent owing to the retrospective nature of the study. Patients who underwent intravenous contrast–enhanced abdominal CT imaging between January 2013 and June 2024 for any clinical indication were included (Figure 1). We initially screened 41,163 scans. For individuals with multiple scans, only the earliest examination was retained, resulting in the exclusion of 11,613 repeat scans. A previously validated algorithm[58] was used to determine the portal venous contrast phase of the scans, and 4,160 subjects without portal venous phase scanning were excluded. An additional 2,469 cases were excluded due to missing height data, along with 1 patient height outlier (< 100 cm). 141 patients under the age of 18 years were excluded. Finally, 62 patients with unusable mortality data (58 deaths without a recorded date and 4 deaths recorded before the scan), 2 with missing BMI and 5 without segmented subcutaneous adipose tissue were excluded. International Classification of Diseases (ICD-9 and ICD-10) diagnosis codes were extracted from the EHR if recorded within a predefined temporal window spanning 1 year prior to and up to 3 months following the index CT examination. Demographic and clinical variables were obtained from the EHR, including age at imaging, sex, race and ethnicity, BMI, height, weight and ICD diagnosis codes. Cohort demographics are summarized in Table 1.

CT image processing and metric derivation

CT scans were obtained on scanners from four manufacturers (9,471 scans on GE, 7,183 on Siemens, 6,054 on Toshiba and 2 on Philips). CT acquisition parameters included a median tube voltage of 120 kV (range, 70-140 kV), a median slice thickness of 1 mm (range, 0.5-5 mm), and an effective tube current setting based on patient attenuation using standard dose modulation.

Body composition metrics were derived with Comp2Comp, an open-source, previously validated deep learning pipeline[22,59,60]. Definitions for the extraction of body composition metrics, including relevant code, training set, and validation, have been detailed previously[59].

An axial slice at the level of the third lumbar vertebra (L3) was first isolated for each CT scan, as this anatomic level has been extensively validated in the literature as a representative site for estimating whole-body adipose tissue distribution[61,62]. The L3 slice was selected by a two-dimensional fully convolutional neural network, and the visceral and subcutaneous adipose tissue compartments on this slice were segmented by the Comp2Comp segmentation model[59], enabling quantification of morphological metrics such as cross-sectional area (cm^2) for each tissue type. Each cross-sectional area was then normalized to patient height in meters to derive the SFI [cm^2/m] and VFI [cm^2/m]. Using these same segmentations, we further quantified the density of each compartment by computing the mean attenuation within the segmented regions to derive the SFD and VFD imaging biomarkers. For CT-derived metrics, "density" refers to radiodensity (attenuation) and is measured in Hounsfield Units (HU). Finally, sex-specific z-scores were calculated for each imaging marker by subtracting the sex-specific mean and normalizing by the standard

deviation (summarized in Table 1). Odds ratios therefore represent the change in odds per 1 standard deviation increase in the respective metric.

Mapping diagnosis codes to phenotypes

EHR diagnosis codes were retrieved for all included patients. ICD-9 and ICD-10 codes occurring within 1 year before to 3 months after the CT scan date were included to capture relevant contemporaneous diagnoses. Phecodes are a standardized, hierarchical phenotype classification system derived from ICD codes. This mapping was performed to aggregate thousands of granular ICD diagnosis codes into clinically meaningful phenotype groups ("phecodes"), thereby reducing redundancy and enabling high-throughput association testing across the entire disease spectrum in a standardized manner. ICD diagnosis codes were mapped to phecodes using Phecode Map v1.2 (ICD-9-CM) and its ICD-10-CM beta map as implemented in the R PheWAS package[33,63]. Codes recorded before the ICD-10-CM transition on 1 October 2015 were mapped through ICD-9-CM and later codes through ICD-10-CM; entries listing several codes were split into individual codes, and each diagnosis entry was counted at most once per phecode. ICD codes absent from the phecode map were assigned to their nearest parent code within two characters whose phecode agreed with those of its mapped child codes (2.4% and 5.6% of in-window code occurrences at the two sites), and ICD-10-CM I48.1 (persistent atrial fibrillation), which the map assigns to atrial flutter, was assigned to atrial fibrillation. Individuals with ≥2 occurrences of a phecode were considered cases, those with 0 were controls, and those with 1 occurrence were excluded. The prevalence of tested phecodes is listed in Table 3.

Statistical analysis

We performed a phenome-wide association analysis between sex-specific z-scores of CT-derived adipose metrics and each phecode-defined medical phenotype. Logistic regression models were fit for each phenotype with standardized age, sex, a natural cubic spline for BMI (4 degrees of freedom) and natural cubic splines (3 degrees of freedom each) for log2 tube current, tube voltage and log2 slice thickness as covariates. Analyses were restricted to phenotypes with ≥200 cases and ≥200 controls, yielding 624 eligible phenotypes. Because each phenotype was tested against all four adipose metrics, statistical significance was defined at a Bonferroni-corrected threshold accounting for all 2,496 marker–phenotype tests ($p < 0.05/2{,}496 = 2.0 \times 10^{-5}$). Odds ratios (ORs) are reported with 95% confidence intervals (CIs). Analyses were conducted with the R software package (version 4.5.1).

Concordance analysis of area and density metrics

To compare area- and density-based associations, we restricted the analysis to phenotypes significantly associated with at least one area metric (SFI or VFI) and at least one density metric (SFD or VFD). For each such phenotype, we selected the single area metric and the single density metric with the largest absolute effect size (|log(OR)|) as representative of its class, regardless of its significance (restricting the selection to significant markers did not change any classification). Phenotypes were classified as directionally concordant when the representative area and density metrics conferred risk in the same direction (both OR > 1 or both OR < 1) and discordant when they conferred risk in opposite directions. To quantify the area–density relationship across the whole phenome rather than only within the overlap, we computed the Pearson correlation between the

representative area and density log odds ratios of all 624 tested phenotypes, which is reported descriptively because phenotypes are nested and share patients.

Joint modelling of adipose area and density

To determine whether associations with adipose density were independent of adipose quantity, and vice versa, we fitted for each phenotype a logistic model containing all four markers together with the covariates above. Likelihood-ratio tests assessed the joint contribution of the four markers (4 degrees of freedom; Bonferroni-corrected over 624 phenotypes) and, for phenotypes passing this test, the contribution of the two density markers given the two area markers and of the two area markers given the two density markers (2 degrees of freedom each; Bonferroni-corrected over 1,248 tests). Marker-level conditional odds ratios were estimated from depot-specific models containing the area and density marker of the same depot (Bonferroni-corrected over 2,496 tests). Variance inflation factors were at most 4.6.

Mortality analysis

We evaluated associations between CT-derived adipose biomarkers and all-cause mortality. The index date was the date of the CT examination. Mortality status and date of death were ascertained from the institutional EHR (Epic) and from Social Security Administration death records linked to the institutional research data repository. Participants without a recorded death were administratively censored on November 18, 2024, corresponding to the mortality-data cutoff. Participants missing any required variable were excluded by complete-case analysis. Primary analyses used logistic regression to estimate associations with all-cause mortality within 1 and 5 years after the index CT,

adjusted for standardized age, sex, BMI (natural cubic spline, 4 degrees of freedom), log2 tube current and tube voltage (natural cubic splines, 3 degrees of freedom each) and slice-thickness protocol (1.0 mm, 1.25 mm or other). At each horizon, participants were included if they died by that horizon or had follow-up extending through it. Results are presented as odds ratios (ORs) with 95% confidence intervals (CIs) and two-sided p-values. Conventional Cox models were evaluated but were not used as the primary analysis because Schoenfeld-residual testing rejected the proportional-hazards assumption for every biomarker.

Data Availability

The analysis code and all associations are publicly available: https://atesfet.github.io/fatwas.io. The raw data are not publicly available because they contain protected health information; data that support the findings are available from the corresponding author upon reasonable request.

Acknowledgements

Author Contributions

Conceptualization was led by A.F., J.M.Z.C., A.S.C. and R.D.B. Methodology, investigation and visualization were carried out by A.F., J.M.Z.C. and A.T.F. Statistical methods were validated by T.L. Associations were reviewed by A.F., A.T.F., I.L., R.H., S.A., G.N., A.K., C.P.L., A.T.S., D.J.M., F.R., L.L., A.S.C. and R.D.B. A.S.C. provided resources. A.S.C. and R.D.B. supervised the project. The original manuscript was written by A.F. and A.T.F., and the manuscript was reviewed and edited by all authors.

Funding

Funding for this work was supported by NIH grants R01 HL167974, R01HL169345, and the Stanford Cardiovascular Institute Seed Grant.

Separately, A.C. receives research support from NIH grants R01 AR077604, R01 EB002524, R01 AR079431, P41 EB 027060, P50 HD118632; Advanced Research Projects Agency for Health (ARPA-H) Biomedical Data Fabric (AY2AX000045), Chatbot Accuracy and Reliability Evaluation programs (AYSAX0000024), and Agentic AI-Enabled Cardiovascular Care Transformation (AY2AX000218); and the Medical Imaging and Data Resource Center (MIDRC), which is funded by the National Institute of Biomedical Imaging and Bioengineering (NIBIB) under contract 75N92020C00021 and through ARPA-H.

Unrelated to this work, A.C. receives research support from GE Healthcare, Siemens, Philips, Microsoft, Amazon, Google, NVIDIA, Stability; has provided consulting services to Patient Square Capital, Chondrometrics GmbH, and Elucid Bioimaging; is co-founder of and receives personal fees from Cognita Imaging; has equity interest in Subtle Medical, LVIS Corp, Brain Key, Almanac Health, and Radiology Partners.

Competing Interest

Additional Information

References

1. Nguyen, T. T. & Corvera, S. Adipose tissue as a linchpin of organismal ageing. *Nat. Metab.* **6**, 793–807 (2024).
2. Writing Committee Members *et al.* 2026 AHA/ACC/ADA/ASN Guideline for the Prevention, Detection, Evaluation, and Management of Cardiovascular-Kidney-Metabolic Syndrome: A Report of the American College of Cardiology/American Heart

Association Joint Committee on Clinical Practice Guidelines. *Circulation* **154**, e50–e158.

3. Kong, F. *et al.* Comprehensive evaluation of GLP-1 receptor agonists: an umbrella review of clinical outcomes across multiple diseases. *Nat. Commun.* **17**, 972 (2026).
4. Alkhatib, M. *et al.* The multifaceted effects of semaglutide: exploring its broad therapeutic applications. *Future Sci. OA* **11**, 2483607 (2025).
5. Iwamoto, Y. *et al.* Tirzepatide, a dual glucose-dependent insulinotropic polypeptide/glucagon-like peptide 1 receptor agonist, exhibits favourable effects on pancreatic β-cells and hepatic steatosis in obese type 2 diabetic db/db mice. *Diabetes Obes. Metab.* **26**, 5982–5994 (2024).
6. Newsome, P. N. & Ambery, P. Incretins (GLP-1 receptor agonists and dual/triple agonists) and the liver. *J. Hepatol.* **79**, 1557–1565 (2023).
7. Ma, T. *et al.* Distinct effects of semaglutide and tirzepatide on metabolic and inflammatory gene expression in brown adipose tissue of mice fed a high-fat, high-fructose diet. *Front. Nutr.* **12**, (2025).
8. Pugliese, N. R. *et al.* Refining the link between obesity and heart failure: insights from GLP-1 receptor agonist trials and studies adopting direct adiposity measures. *Cardiovasc. Diabetol.* **24**, 224 (2025).
9. Lee, J. J. *et al.* Cross-Sectional Associations of Computed Tomography (CT)-Derived Adipose Tissue Density and Adipokines: The Framingham Heart Study. *J. Am. Heart Assoc.* **5**, e002545 (2016).

10. Murphy, R. A. *et al.* Adipose Tissue Density, a Novel Biomarker Predicting Mortality Risk in Older Adults. *J. Gerontol. A. Biol. Sci. Med. Sci.* **69**, 109–117 (2014).
11. Kapoor, N. D. *et al.* Adipose tissue density on CT as a prognostic factor in patients with cancer: a systematic review. *Acta Oncol.* **59**, 1488–1495 (2020).
12. Uchida, K. *et al.* Association between abdominal adiposity and cognitive decline in older adults: a 10-year community-based study. *J. Nutr. Health Aging* **28**, 100175 (2024).
13. Zhang, B. *et al.* Quantitative CT Assessment of Skeletal Muscle and Abdominal Fat Distribution: Predictive Value for Type 2 Diabetes Mellitus. *Diabetes Metab. Syndr. Obes.* **18**, 4153–4163 (2025).
14. Eriksen, C. S. & Møller, S. Quantitative Assessment of Body Composition in Cirrhosis. *Diagnostics* **14**, 2191 (2024).
15. Chartrand, D., Almeras, N., Lemieux, I. & Despres, J.-P. Abstract P621: Visceral Adipose Tissue Attenuation: A Marker of Liver Fat Content Beyond the Body Mass Index and Visceral Adipose Tissue Area. *Circulation* **147**, AP621–AP621 (2023).
16. Monirujjaman, M., Martin, L., Stretch, C. & Mazurak, V. C. Adipose Tissue Radiodensity in Chronic Diseases: A Literature Review of the Applied Methodologies. *Immunometabolism* **3**, e210033 (2021).
17. Atçeken, Z. *et al.* Subcutaneous Fat Tissue Density as a Novel Diagnostic Indicator in Distinguishing Pulmonary Edema from Viral Pneumonias: A Retrospective Cross-Sectional Study. *Turk. Klin. Arch. Lung* **24**, 25–31 (2025).

18. Kaess, B. M. *et al*. The ratio of visceral to subcutaneous fat, a metric of body fat distribution, is a unique correlate of cardiometabolic risk. *Diabetologia* **55**, 2622–2630 (2012).
19. Yun, C.-H. *et al*. The Normal Limits, Subclinical Significance, Related Metabolic Derangements and Distinct Biological Effects of Body Site-Specific Adiposity in Relatively Healthy Population. *PLOS ONE* **8**, e61997 (2013).
20. Bosch, T. A. *et al*. Visceral adipose tissue measured by DXA correlates with measurement by CT and is associated with cardiometabolic risk factors in children. *Pediatr. Obes.* **10**, 172–179 (2015).
21. Ohashi, N. *et al*. Association Between Visceral Adipose Tissue Area and Coronary Plaque Morphology Assessed by CT Angiography. *JACC Cardiovasc. Imaging* **3**, 908–917 (2010).
22. Zambrano Chaves, J. M. *et al*. Opportunistic assessment of ischemic heart disease risk using abdominopelvic computed tomography and medical record data: a multimodal explainable artificial intelligence approach. *Sci. Rep.* **13**, 21034 (2023).
23. Pickhardt, P. J. *et al*. Automated CT biomarkers for opportunistic prediction of future cardiovascular events and mortality in an asymptomatic screening population: a retrospective cohort study. *Lancet Digit. Health* **2**, e192–e200 (2020).
24. Lake, J. E. *et al*. CT Fat Density Accurately Reflects Histologic Fat Quality in Adults With HIV On and Off Antiretroviral Therapy. *J. Clin. Endocrinol. Metab.* **104**, 4857–4864 (2019).

25. Kuchnia, A. J. *et al.* Automated CT-based visceral fat density predicts mortality regardless of visceral fat area. *Br. J. Radiol.* tqag001 (2026) doi:10.1093/bjr/tqag001.
26. Cheng, E. *et al.* Adipose tissue radiodensity and mortality among patients with nonmetastatic breast cancer. *Clin. Nutr. Edinb. Scotl.* **41**, 2607–2613 (2022).
27. Gaborit, B. & Dutour, A. Looking beyond ectopic fat amount: A SMART method to quantify epicardial adipose tissue density. *Eur. J. Prev. Cardiol.* **24**, 657–659 (2017).
28. Ebadi, M. *et al.* Higher subcutaneous adipose tissue radiodensity is associated with increased mortality in patients with cirrhosis. *JHEP Rep.* **4**, 100495 (2022).
29. Feliciano, E. M. C. *et al.* Abdominal adipose tissue radiodensity is associated with survival after colorectal cancer. *Am. J. Clin. Nutr.* **114**, 1917–1924 (2021).
30. Haidar, A. *et al.* Abstract 12439: Abdominal Visceral Fat Area and Density Are Associated With Coronary Artery Calcification: A Cross-Sectional Analysis of the Multi-Ethnic Study of Atherosclerosis. *Circulation* **148**, A12439–A12439 (2023).
31. Bastarache, L., Denny, J. C. & Roden, D. M. Phenome-Wide Association Studies. *JAMA* **327**, 75–76 (2022).
32. Doss, J., Mo, H., Carroll, R. J., Crofford, L. J. & Denny, J. C. Phenome-Wide Association Study of Rheumatoid Arthritis Subgroups Identifies Association Between Seronegative Disease and Fibromyalgia. *Arthritis Rheumatol.* **69**, 291–300 (2017).
33. Carroll, R. J., Bastarache, L. & Denny, J. C. R PheWAS: data analysis and plotting tools for phenome-wide association studies in the R environment. *Bioinformatics* **30**, 2375–2376 (2014).

34. Zambrano Chaves, J. M. *et al.* Abdominal CT metrics in 17,646 patients reveal associations between myopenia, myosteatosis, and medical phenotypes: a phenome-wide association study. *eBioMedicine* **103**, 105116 (2024).
35. Gómez-Banoy, N. *et al.* Artificial intelligence-enabled clinical phenotyping of human brown fat. *Nature* 1–10 (2026) doi:10.1038/s41586-026-11162-7.
36. Kubota, S. & Yabe, D. Visceral Adipose Tissue Quality and its Impact on Metabolic Health. *J. Clin. Endocrinol. Metab.* **109**, e1665–e1666 (2024).
37. Bates, D. D. B. & Pickhardt, P. J. CT-Derived Body Composition Assessment as a Prognostic Tool in Oncologic Patients: From Opportunistic Research to Artificial Intelligence–Based Clinical Implementation. *Am. J. Roentgenol.* **219**, 671–680 (2022).
38. Shi, J. *et al.* Deciphering CT texture features of human visceral fat to evaluate metabolic disorders and surgery-induced weight loss effects. *eBioMedicine* **69**, (2021).
39. Tapper, E. B. *et al.* Body composition predicts mortality and decompensation in compensated cirrhosis patients: A prospective cohort study. *JHEP Rep. Innov. Hepatol.* **2**, 100061 (2020).
40. Ha, N. B. *et al.* Visceral Adipose Tissue Inflammation and Radiographic Visceral-to-Subcutaneous Adipose Tissue Ratio in Patients with Cirrhosis. *Dig. Dis. Sci.* **67**, 3436–3444 (2022).
41. Babic, A. *et al.* Adipose tissue and skeletal muscle wasting precede clinical diagnosis of pancreatic cancer. *Nat. Commun.* **14**, 4317 (2023).

42. van Dijk, D. P. J. *et al.* Low skeletal muscle radiation attenuation and visceral adiposity are associated with overall survival and surgical site infections in patients with pancreatic cancer. *J. Cachexia Sarcopenia Muscle* **8**, 317–326 (2017).
43. Wang, Z. *et al.* Looking at or beyond the tumor - a systematic review and meta-analysis of quantitative imaging biomarkers predicting pancreatic cancer prognosis. *Abdom. Radiol.* **50**, 4646–4660 (2025).
44. Yamamoto, A. *et al.* Imaging spectrum of abnormal subcutaneous and visceral fat distribution. *Insights Imaging* **11**, 24 (2020).
45. Ishikawa, R. *et al.* Association Between Subcutaneous Adipose Tissue Radiodensity and All-Cause Mortality in Patients Undergoing Hemodialysis: A Retrospective Cohort Study. *J. Ren. Nutr.* **0**, (2026).
46. Stello, B. B. *et al.* Concurrent and predictive validity of different tools for malnutrition diagnosis in adult critically ill patients: a systematic review with meta-analysis of observational studies. *Am. J. Clin. Nutr.* **123**, 101195 (2026).
47. Blankemeier, L. *et al.* Opportunistic Incidence Prediction of Multiple Chronic Diseases from Abdominal CT Imaging Using Multi-task Learning. in *Medical Image Computing and Computer Assisted Intervention – MICCAI 2022* (eds Wang, L., Dou, Q., Fletcher, P. T., Speidel, S. & Li, S.) 309–318 (Springer Nature Switzerland, Cham, 2022). doi:10.1007/978-3-031-16449-1_30.
48. Blankemeier, L. *et al.* Merlin: a computed tomography vision–language foundation model and dataset. *Nature* **652**, 1318–1328 (2026).

49. Jayedi, A., Khan, T. A., Aune, D., Emadi, A. & Shab-Bidar, S. Body fat and risk of all-cause mortality: a systematic review and dose-response meta-analysis of prospective cohort studies. *Int. J. Obes.* **46**, 1573–1581 (2022).
50. Lee, S. W. *et al.* Body fat distribution is more predictive of all-cause mortality than overall adiposity. *Diabetes Obes. Metab.* **20**, 141–147 (2018).
51. Saad, R. K. *et al.* Abdominal Visceral Adipose Tissue and All-Cause Mortality: A Systematic Review. *Front. Endocrinol.* **13**, (2022).
52. Ebner, N. *et al.* Mechanism and novel therapeutic approaches to wasting in chronic disease. *Maturitas* **75**, 199–206 (2013).
53. Braun, T. P. & Marks, D. L. Pathophysiology and treatment of inflammatory anorexia in chronic disease. *J. Cachexia Sarcopenia Muscle* **1**, 135–145 (2010).
54. Daas, S. I., Rizeq, B. R. & Nasrallah, G. K. Adipose tissue dysfunction in cancer cachexia. *J. Cell. Physiol.* **234**, 13–22 (2019).
55. Becher, T. *et al.* Brown adipose tissue is associated with cardiometabolic health. *Nat. Med.* **27**, 58–65 (2021).
56. Cypess, A. M. *et al.* Identification and Importance of Brown Adipose Tissue in Adult Humans. *N. Engl. J. Med.* **360**, 1509–1517 (2009).
57. Littlejohns, T. J. *et al.* The UK Biobank imaging enhancement of 100,000 participants: rationale, data collection, management and future directions. *Nat. Commun.* **11**, 2624 (2020).

58. Reis, E. P. *et al.* Automated abdominal CT contrast phase detection using an interpretable and open-source artificial intelligence algorithm. *Eur. Radiol.* **34**, 6680–6687 (2024).
59. Rao, A. *et al.* Comp2Comp: Open-Source Software with FDA-Cleared Artificial Intelligence Algorithms for Computed Tomography Image Analysis. Preprint at https://doi.org/10.48550/arXiv.2602.10364 (2026).
60. Blankemeier, L. *et al.* Comp2Comp: Open-Source Body Composition Assessment on Computed Tomography. Preprint at https://doi.org/10.48550/arXiv.2302.06568 (2023).
61. Hong, J. H. *et al.* CT analysis of thoracolumbar body composition for estimating whole-body composition. *Insights Imaging* **14**, 69 (2023).
62. Jeong, D. *et al.* Comparison of volumetric and single-slice computed tomography body composition metrics for colorectal cancer survival. *Eur. J. Radiol.* **190**, 112241 (2025).
63. Wu, P. *et al.* Mapping ICD-10 and ICD-10-CM Codes to Phecodes: Workflow Development and Initial Evaluation. *JMIR Med. Inform.* **7**, e14325 (2019).

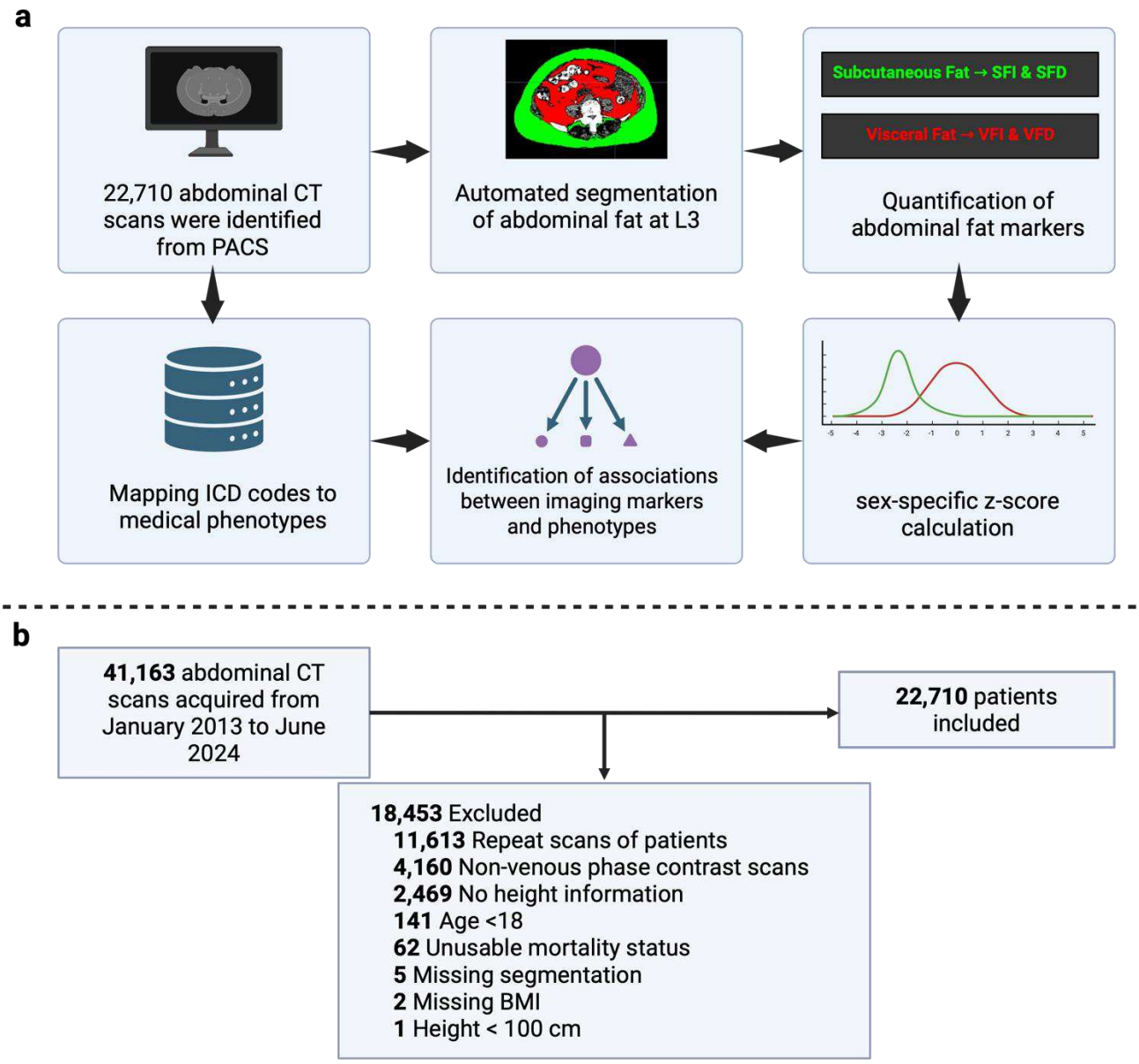
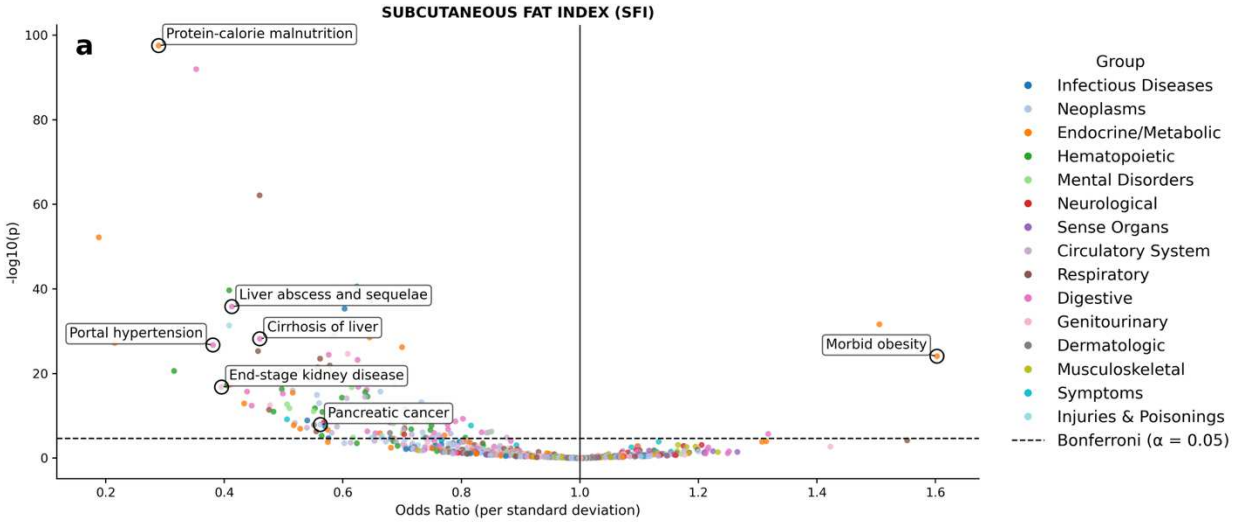
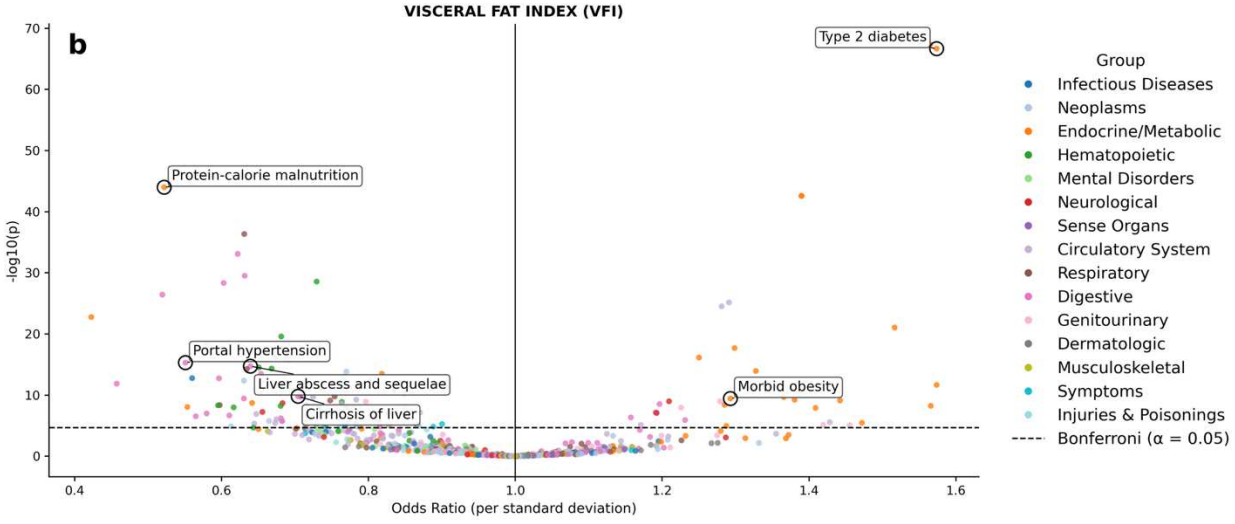


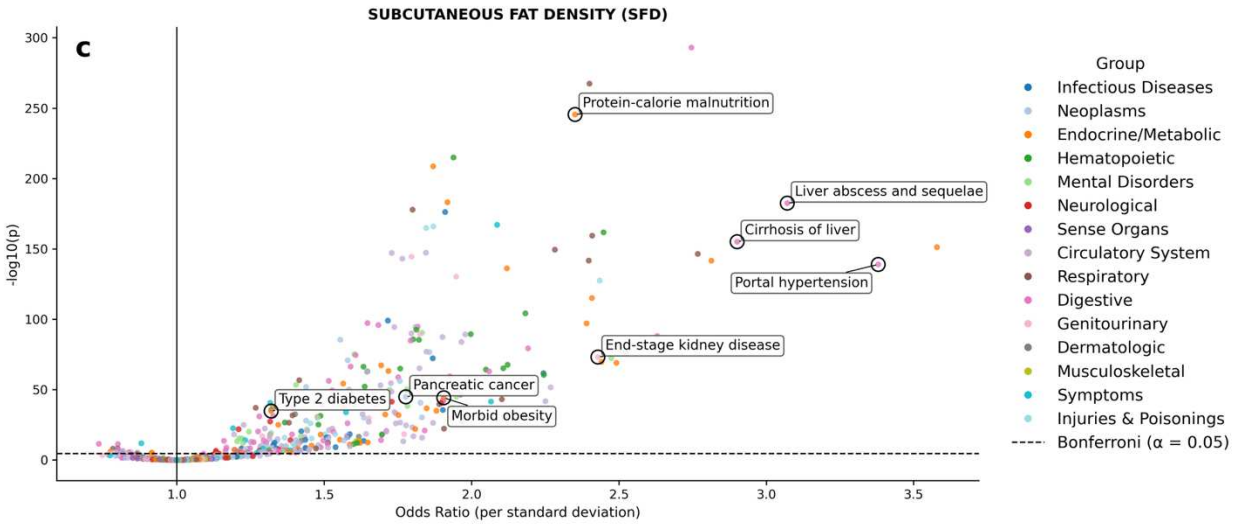
Figure 1. (a) Study design overview and (b) flowchart of patient inclusion and exclusion criteria. CT, computed tomography; PACS, picture archiving and communications system; SFI, subcutaneous fat index; SFD, subcutaneous fat density; VFI, visceral fat index; VFD, visceral fat density; ICD, International Classification of Diseases.


SUBCUTANEOUS FAT INDEX (SFI)
a
Protein-calorie malnutrition
Liver abscess and sequelae
Cirrhosis of liver
Portal hypertension
End-stage kidney disease
Pancreatic cancer
Morbid obesity
-log10(p)
Odds Ratio (per standard deviation)
Group
Infectious Diseases
Neoplasms
Endocrine/Metabolic
Hematopoietic
Mental Disorders
Neurological
Sense Organs
Circulatory System
Respiratory
Digestive
Genitourinary
Dermatologic
Musculoskeletal
Symptoms
Injuries & Poisonings
Bonferroni (α = 0.05)

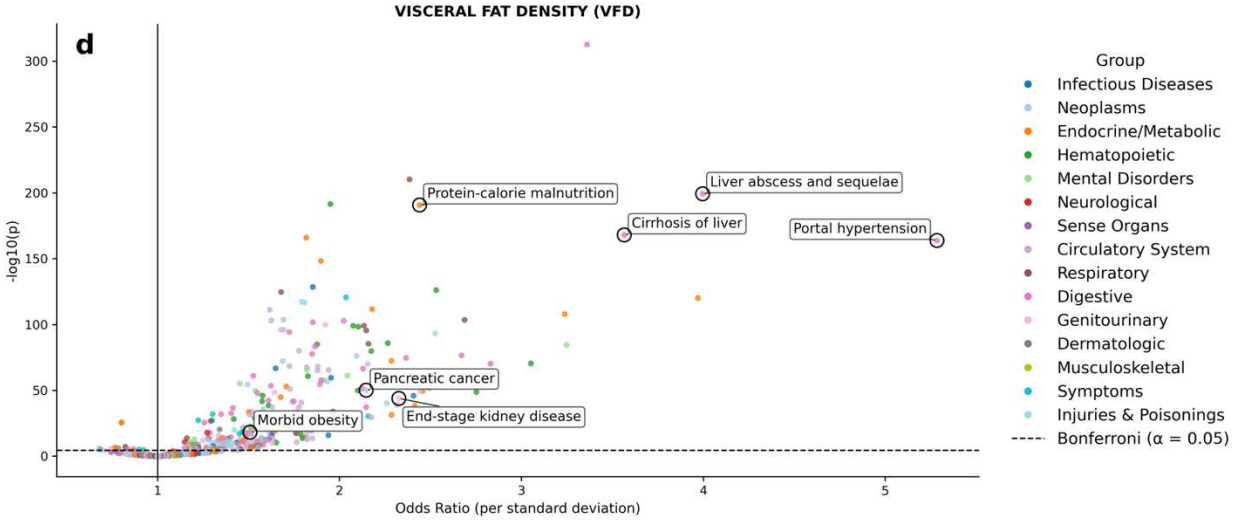
739


VISCERAL FAT INDEX (VFI)
b
Type 2 diabetes
Protein-calorie malnutrition
Portal hypertension
Liver abscess and sequelae
Cirrhosis of liver
Morbid obesity
-log10(p)
Odds Ratio (per standard deviation)
Group
Infectious Diseases
Neoplasms
Endocrine/Metabolic
Hematopoietic
Mental Disorders
Neurological
Sense Organs
Circulatory System
Respiratory
Digestive
Genitourinary
Dermatologic
Musculoskeletal
Symptoms
Injuries & Poisonings
Bonferroni (α = 0.05)

740



741



742

743 **Figure 2. Volcano plots of odds ratios versus significance for CT-derived fat metrics.** (a)
744 SFI, (b) VFI, (c) SFD, (d) VFD. The two congenital-anomaly phenotypes (neither significant)
745 are not shown. The dashed line indicates the Bonferroni-corrected significance threshold.
746 Labels identify the Table 4 phenotypes that reached the Bonferroni-corrected threshold for
747 the metric shown; a Table 4 phenotype is left unlabelled in a panel when it was not significant
748 for that metric. An interactive version of these plots is available online
749 (https://atesfet.github.io/fatwas.io), enabling detailed exploration of all phenotype-level
750 associations.

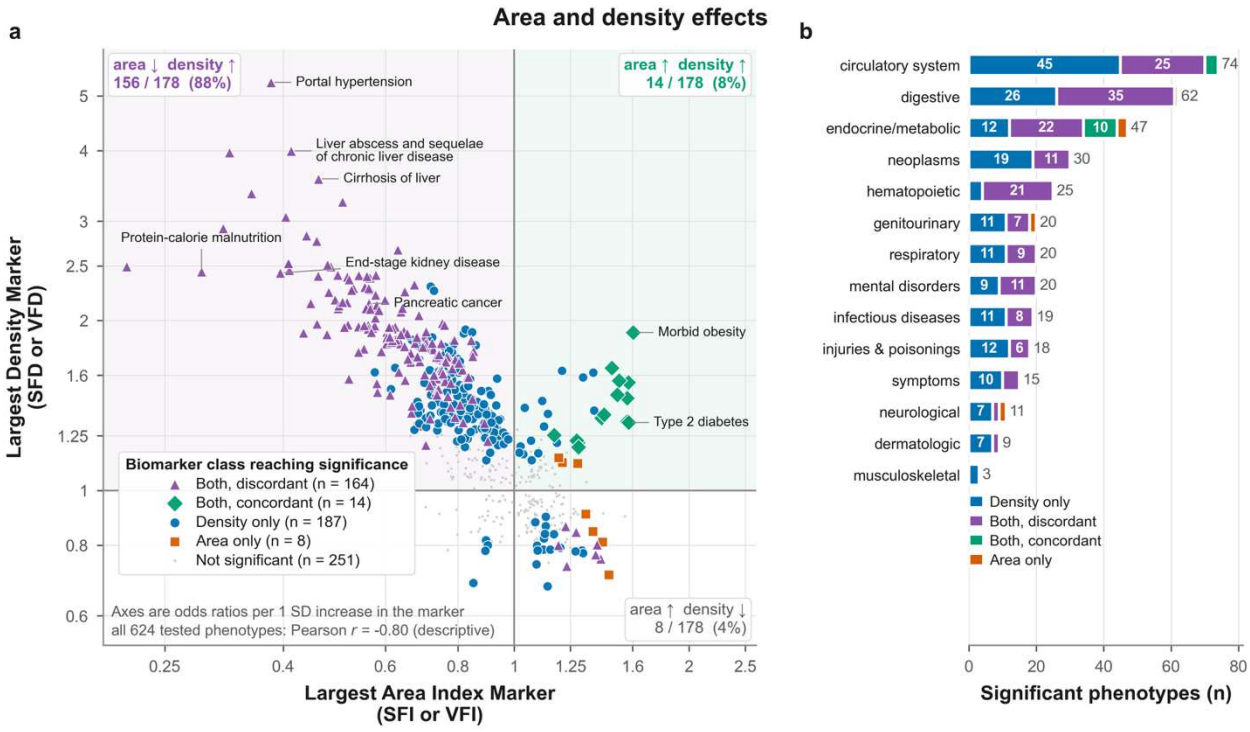
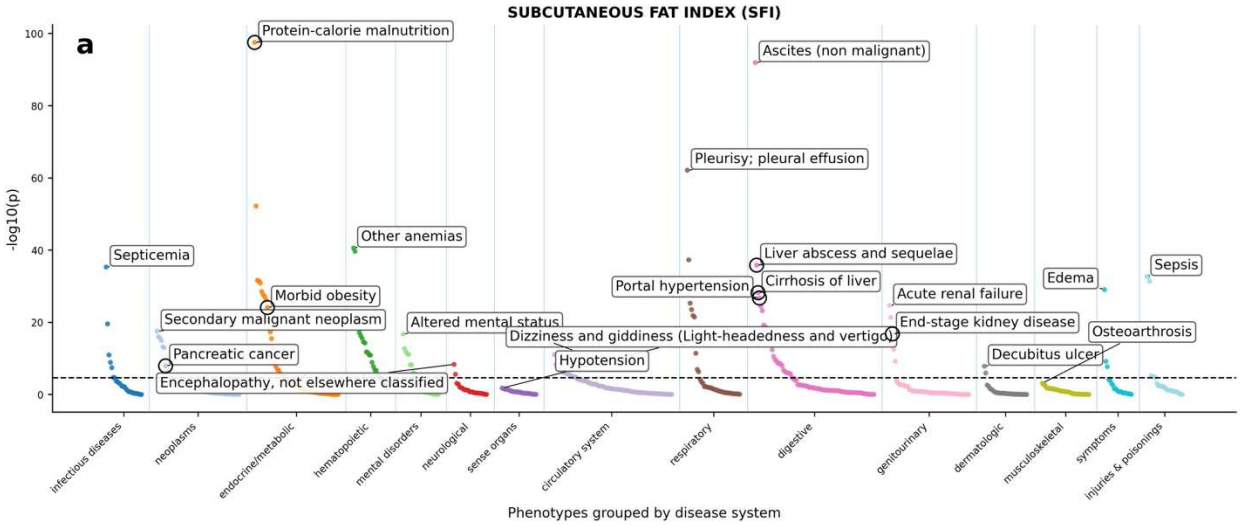
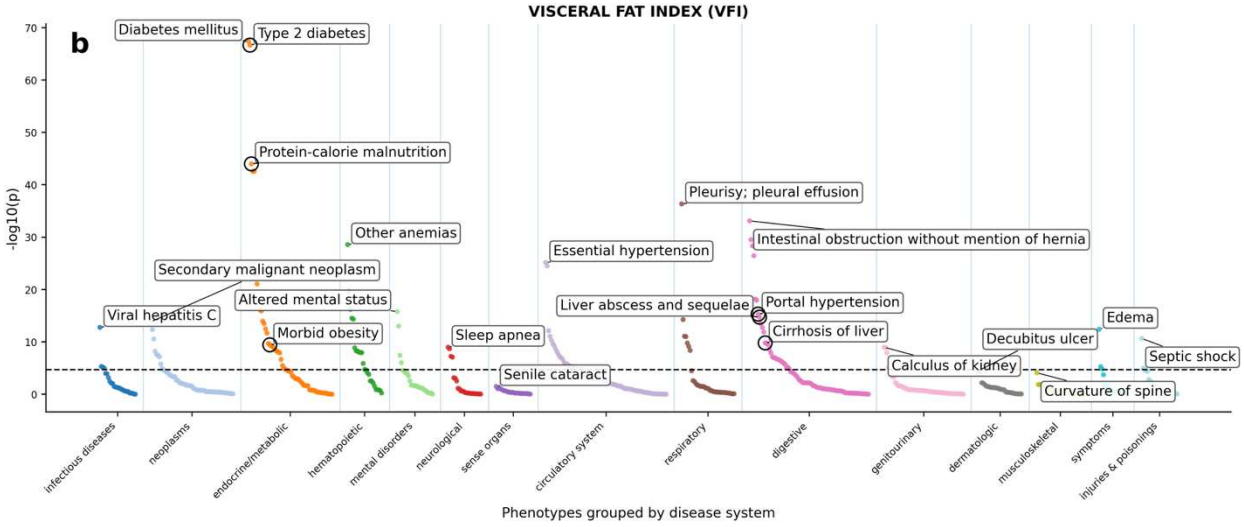


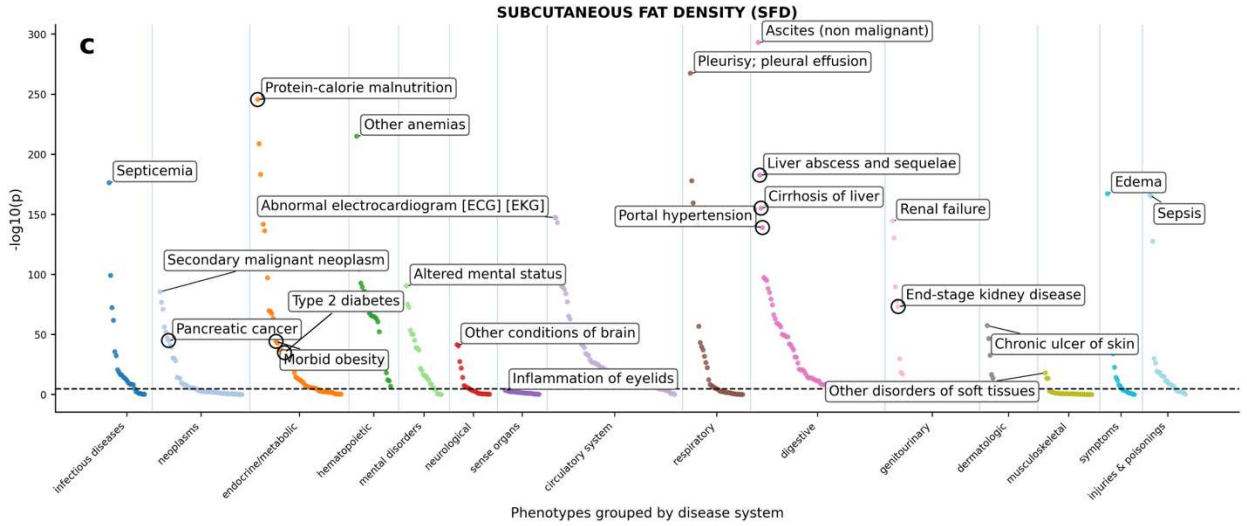
Figure 3. Adipose area and density odds ratios are inversely related across the phenome, and density-only associations occur in every disease group with a significant association. (a) Each of the 624 tested phenotypes plotted by the odds ratio of the area-index marker with the largest absolute log odds ratio (x axis; SFI or VFI) against the density marker with the largest absolute log odds ratio (y axis; SFD or VFD), per one sex-specific standard-deviation increase, adjusted for age, sex, BMI and CT acquisition parameters (n = 22,710 patients). Color and symbol give which biomarker class passed the Bonferroni-corrected threshold ($p < 2.0 \times 10^{-5}$); boxed values partition the 178 phenotypes significant for both classes across the quadrants. Labelled points are the phenotypes of Table 4. Across all 624 phenotypes, the representative area and density log odds ratios were inversely correlated (Pearson r = −0.80; descriptive, because phenotypes are nested and share patients). (b) Bonferroni-significant phenotypes per disease group in the same four classes.


SUBCUTANEOUS FAT INDEX (SFI)
a
-log10(p)
Protein-calorie malnutrition
Ascites (non malignant)
Pleurisy; pleural effusion
Other anemias
Septicemia
Liver abscess and sequelae
Sepsis
Edema
Portal hypertension
Cirrhosis of liver
Morbid obesity
Acute renal failure
Secondary malignant neoplasm
Altered mental status
End-stage kidney disease
Osteoarthrosis
Dizziness and giddiness (Light-headedness and vertigo)
Pancreatic cancer
Hypotension
Decubitus ulcer
Encephalopathy, not elsewhere classified
infectious diseases
neoplasms
endocrine/metabolic
hematopoietic
mental disorders
neurological
sense organs
circulatory system
respiratory
digestive
genitourinary
dermatologic
musculoskeletal
symptoms
injuries & poisonings
Phenotypes grouped by disease system

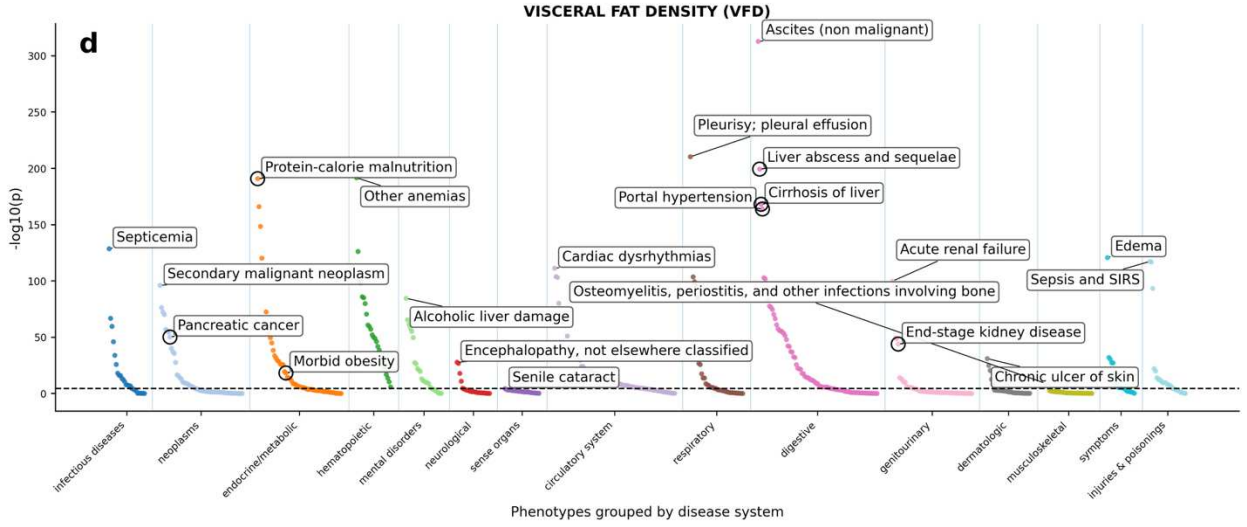
765


VISCERAL FAT INDEX (VFI)
b
-log10(p)
Diabetes mellitus
Type 2 diabetes
Protein-calorie malnutrition
Pleurisy; pleural effusion
Other anemias
Intestinal obstruction without mention of hernia
Essential hypertension
Secondary malignant neoplasm
Altered mental status
Liver abscess and sequelae
Portal hypertension
Viral hepatitis C
Cirrhosis of liver
Edema
Morbid obesity
Sleep apnea
Decubitus ulcer
Septic shock
Calculus of kidney
Senile cataract
Curvature of spine
infectious diseases
neoplasms
endocrine/metabolic
hematopoietic
mental disorders
neurological
sense organs
circulatory system
respiratory
digestive
genitourinary
dermatologic
musculoskeletal
symptoms
injuries & poisonings
Phenotypes grouped by disease system

766



767



768

769 **Figure 4. Manhattan plots of phenome-wide associations for CT-derived fat metrics.**

770 (a) SFI, (b) VFI, (c) SFD, (d) VFD. Each point represents a phecode-level association, with

771 significance plotted as $-\log_{10}(p)$. Higher values indicate stronger statistical evidence of

772 association, irrespective of direction; phenotypes are grouped by disease group. Dashed

773 line marks the Bonferroni-corrected significance threshold ($p < 0.05/2,496$). Labels identify

774 the most significant phenotype in each disease group together with the Table 4 phenotypes

775 that reached the Bonferroni-corrected threshold for the metric shown. The two congenital-

776 anomaly phenotypes (neither significant) are not shown.

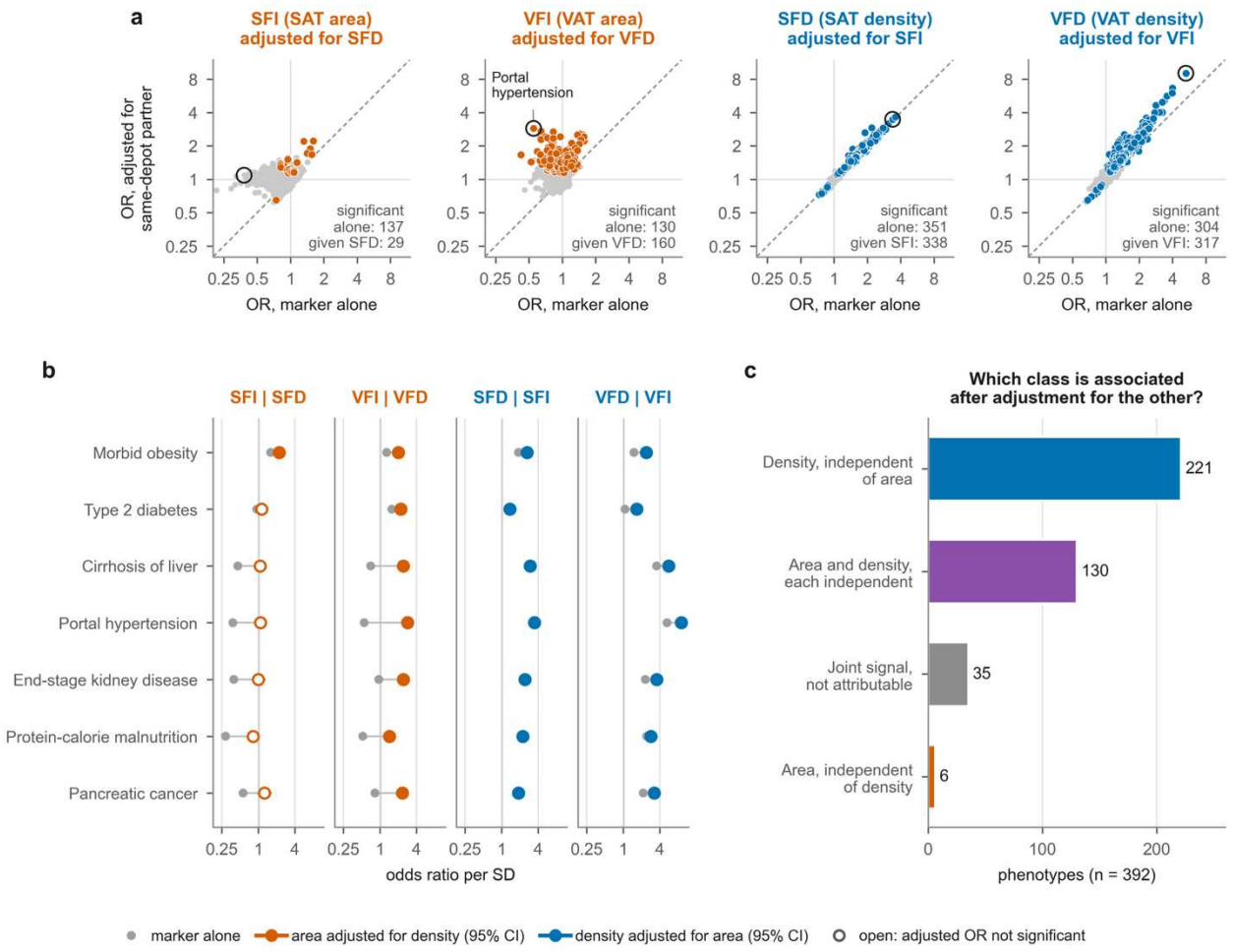


Figure 5. Joint modelling separates adipose composition from adipose quantity. (a) For each of the 624 tested phenotypes, the odds ratio of each marker alone (x axis) against its odds ratio after adjustment for the other marker of the same depot (y axis; SFI with SFD, VFI with VFD). Points on the dashed line are unchanged by adjustment; colored points are Bonferroni-significant after adjustment ($p < 0.05/2{,}496$), and the counts give the number of phenotypes significant for the marker alone and the number significant after adjustment (including phenotypes not significant alone). Density associations lie close to the line, subcutaneous area associations largely move toward 1, and visceral area associations lie above 1 at a given visceral density. The ringed point is portal hypertension. (b) Odds ratios for seven of the Table 4 phenotypes for the marker alone (grey) and after adjustment for the

same-depot partner (colored, with 95% CI; open symbols are not significant after adjustment). (c) Attribution of the 392 phenotypes with a joint association of the four markers (4-degree-of-freedom likelihood-ratio test, $p < 0.05/624$): density associated after adjustment for both area markers, area associated after adjustment for both density markers (2-degree-of-freedom tests, $p < 0.05/1{,}248$), both, or neither (joint signal not attributable to either class). Odds ratios are per one sex-specific standard deviation, adjusted for age, sex, BMI and CT acquisition parameters (n = 22,710 patients).

Parameter	Overall (N = 22,710)	Male (n = 9,592)	Female (n = 13,118)	P value
Age [years]	56.32 ± 18.32	56.52 ± 18.07	56.18 ± 18.50	0.166
BMI [kg/m^2]	27.34 ± 6.85	27.15 ± 5.91	27.48 ± 7.47	<0.001
Race/Ethnicity				
Asian	3,499 (15.4%)	1,492 (15.6%)	2,007 (15.3%)	0.599
Black	1,093 (4.8%)	429 (4.5%)	664 (5.1%)	0.040
White	11,581 (51.0%)	5,127 (53.5%)	6,454 (49.2%)	<0.001
Pacific Islander	271 (1.2%)	79 (0.8%)	192 (1.5%)	<0.001
Native American	68 (0.3%)	30 (0.3%)	38 (0.3%)	0.753
Other	1,691 (7.4%)	755 (7.9%)	936 (7.1%)	0.037
Unknown	278 (1.2%)	121 (1.3%)	157 (1.2%)	0.662
Hispanic	4,229 (18.6%)	1,559 (16.3%)	2,670 (20.4%)	<0.001
CT Imaging Metrics				
SFI [cm^2/m]	127.05 ± 84.36	99.85 ± 64.39	146.95 ± 91.39	<0.001
VFI [cm^2/m]	81.44 ± 61.43	101.24 ± 67.73	66.95 ± 51.79	<0.001
SFD [HU]	-94.83 ± 14.19	-92.76 ± 14.92	-96.35 ± 13.42	<0.001
VFD [HU]	-82.35 ± 12.65	-83.48 ± 13.00	-81.52 ± 12.32	<0.001

Table 1. Demographic and clinical characteristics of the study cohort. Continuous variables are mean ± standard deviation; categorical variables are n (%). P values are from Welch's t-test for continuous variables and a two-proportion z-test for categorical variables, comparing men with women.

Metric	18–29	30–39	40–49	50–59	60–69	70–79	80+
Number of females	1288	1610	2068	2378	2435	1939	1400
Number of males	927	1131	1319	1813	1976	1497	929
SFI females [cm^2/m]	147.6 ± 108.6	165.0 ± 106.6	155.6 ± 96.2	155.8 ± 90.0	149.7 ± 86.5	133.4 ± 74.5	111.7 ± 64.3
SFI males [cm^2/m]	94.2 ± 85.6	109.9 ± 76.0	110.7 ± 69.7	106.7 ± 66.5	98.1 ± 56.1	90.6 ± 48.2	83.2 ± 41.1
VFI females [cm^2/m]	36.7 ± 33.3	52.8 ± 42.2	60.3 ± 46.6	73.8 ± 54.5	79.2 ± 54.6	79.6 ± 56.6	70.6 ± 50.0
VFI males [cm^2/m]	46.8 ± 42.4	76.7 ± 53.3	96.8 ± 58.1	108.7 ± 65.9	115.4 ± 69.7	119.9 ± 72.8	117.2 ± 70.1
SFD females [HU]	-97.0 ± 10.9	-97.8 ± 11.6	-97.5 ± 12.6	-98.2 ± 13.0	-96.7 ± 14.0	-94.8 ± 14.9	-90.9 ± 14.6
SFD males [HU]	-91.5 ± 16.1	-95.5 ± 13.6	-95.0 ± 14.1	-94.1 ± 15.8	-92.3 ± 14.7	-91.0 ± 14.8	-88.8 ± 14.1
VFD females [HU]	-77.9 ± 11.4	-81.0 ± 12.1	-81.8 ± 12.1	-83.5 ± 12.3	-82.8 ± 12.5	-81.9 ± 12.6	-78.9 ± 12.0
VFD males [HU]	-79.4 ± 13.6	-85.1 ± 12.0	-85.7 ± 12.6	-84.8 ± 13.2	-83.5 ± 13.1	-82.7 ± 12.8	-81.2 ± 12.5
BMI females [kg/m^2]	27.5 ± 8.1	29.0 ± 8.2	28.5 ± 7.8	28.2 ± 7.6	27.7 ± 7.4	26.5 ± 6.5	24.3 ± 5.4
BMI males [kg/m^2]	26.3 ± 6.5	28.0 ± 6.5	28.5 ± 6.1	28.1 ± 6.3	27.1 ± 5.5	26.2 ± 5.0	24.8 ± 4.4

Table 2. CT-derived adipose tissue metrics of area and density stratified by age and sex. Mean ± standard deviation.

Group	Number of medical phenotypes	Average number of cases/Total number of patients	Prevalence (%) [95% CI]
Circulatory system	86	988/18,054	5.6 [4.0–7.1]
Congenital anomalies	2	232/22,388	1.0 [0.9–1.1]
Dermatologic	31	502/21,489	2.3 [1.8–2.8]
Digestive	85	1,060/17,320	6.4 [5.1–7.7]
Endocrine/ metabolic	60	1,134/19,615	5.7 [4.1–7.3]
Genitourinary	57	781/16,154	4.9 [4.0–5.8]
Hematopoietic	25	945/17,695	5.2 [3.7–6.8]
Infectious diseases	26	575/20,368	2.8 [1.8–3.8]
Injuries & poisonings	26	721/19,382	3.7 [2.7–4.8]
Mental disorders	26	1,096/18,542	5.9 [4.0–7.8]
Musculoskeletal	34	704/20,912	3.3 [2.4–4.3]
Neoplasms	59	636/18,492	3.6 [3.0–4.3]
Neurological	24	1,022/20,485	5.0 [3.1–7.0]
Respiratory	38	989/19,545	5.1 [3.3–6.8]
Sense organs	25	491/21,903	2.2 [1.7–2.8]
Symptoms	20	2,043/21,535	9.6 [2.5–16.7]

Table 3. Prevalence of phecode phenotypes included in the PheWAS analysis. Prevalence is the mean of the per-phenotype prevalences (cases/total) within each group; the 95% CI is the mean ± 1.96 × standard error across the phenotypes of the group.

	SFI	VFI	SFD	VFD
Morbid obesity	1.60* [1.47 - 1.75]	1.29* [1.19 - 1.40]	1.91* [1.74 - 2.08]	1.51* [1.38 - 1.65]
Pancreatic cancer	0.56* [0.46 - 0.68]	–	1.78* [1.64 - 1.92]	2.15* [1.94 - 2.37]
Type 2 diabetes	–	1.57* [1.50 - 1.66]	1.32* [1.26 - 1.38]	–
Cirrhosis of liver without mention of alcohol	0.46* [0.40 - 0.53]	0.70* [0.63 - 0.78]	2.90* [2.68 - 3.14]	3.56* [3.26 - 3.90]
Protein-calorie malnutrition	0.29* [0.26 - 0.32]	0.52* [0.48 - 0.57]	2.35* [2.24 - 2.47]	2.44* [2.30 - 2.59]
Portal hypertension	0.38* [0.32 - 0.45]	0.55* [0.48 - 0.64]	3.38* [3.08 - 3.72]	5.28* [4.70 - 5.96]
Liver abscess and sequelae of chronic liver disease	0.41* [0.36 - 0.47]	0.64* [0.57 - 0.71]	3.07* [2.85 - 3.32]	4.00* [3.65 - 4.37]
End-stage kidney disease	0.40* [0.32 - 0.49]	–	2.43* [2.21 - 2.67]	2.33* [2.07 - 2.62]

Table 4. Selected associations with established prior evidence for SFI, VFI, SFD and VFD. * $p < 0.0001$ (Bonferroni-significant); – not significant at the Bonferroni threshold. We highlight eight representative phenotypes that are strongly associated in our dataset and supported by prior imaging and epidemiologic literature linking adiposity and adipose composition to metabolic, hepatic, renal, oncologic and nutritional disease.